Solar Energy Materials & Solar Cells 264 (2024) 112604

Contents lists available at ScienceDirect

Solar Energy Materials and Solar Cells

journal homepage: www.elsevier.com/locate/solmat

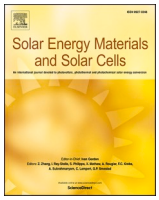

Addressing sodium ion-related degradation in SHJ cells by the application of nano-scale barrier layers

Xinyuan Wu [a], Chandany Sen [a,*], Haoran Wang [a], Xutao Wang [a], Yutong Wu [b], Muhammad Umair Khan [a], Lizhong Mao [b], Fangdan Jiang [b], Tao Xu [b], Guangchun Zhang [b], Bram Hoex [a,**]

[a] School of Photovoltaic and Renewable Energy Engineering, University of New South Wales, Sydney, 2052, Australia
[b] Canadian Solar Inc., Suzhou, Jiangsu, 215129, China

ARTICLE INFO

Keywords:
Silicon heterojunction solar cells
Reliability
Damp-heat stability
Sodium-related degradation
Atomic layer deposition
Aluminium oxide

ABSTRACT

Silicon heterojunction (SHJ) solar cells are renowned for their high efficiency. However, SHJ solar cells are susceptible to various contaminants, leading to significant performance degradation when exposed to damp-heat conditions (e.g., 85 °C and 85% relative humidity). Sodium (Na) has been identified as one of the main contributors to degradation in silicon solar modules subjected to damp-heat conditions. This work investigates the role of an ultra-thin AlO_x capping layer (~10 nm) in preventing the failure in SHJ cells caused by Na-related contaminants. NaCl is applied directly to the solar cell, and the unencapsulated cell undergoes a damp heat test at 85 °C and 85% relative humidity (DH85). It is found that without the AlO_x barrier layer, the SHJ cells experience a relative reduction in power of ~30%$_{rel}$ after only 20 h at DH85. Both the front and rear sides of the cell degrade when exposed to NaCl. This is primarily due to a deterioration of the Ag contact resulting in increased series resistance (R_s), and decrease in fill factor (*FF*), and an increase in recombination, leading to a significant drop in open-circuit voltage (V_{oc}), particularly when NaCl is applied on the rear side. However, when an AlO_x barrier layer is applied to the SHJ cells, the performance losses caused by NaCl are significantly reduced to only ~3.3%$_{rel}$. The loss in V_{oc} on the rear side is completely suppressed, and there is only a slight increase in R_s of ~50%$_{rel}$ compared to ~300%$_{rel}$ increase in R_s for cells without the AlO_x barrier layer. These findings indicate that the ultra-thin AlO_x barrier layer provides effective protection for SHJ cells against Na ions, mitigating both R_s and recombination losses. This AlO_x barrier layer depositing method is compatible with existing industrial mass-production ALD tools and thus presents a viable solution at the cell level for SHJ cells.

1. Introduction

After the successful implementation of the passivated emitter and rear cell (PERC) technology in the solar industry in the mid-2010s, extensive research and development have focused on the next-generation silicon solar cells with at least one full area passivating contact (e.g., tunnelling oxide passivated contact (TOPCon) and silicon heterojunction (SHJ) solar cells [1–5]). SHJ solar cells have achieved remarkable power conversion efficiency (*PCE*) records, with Longi setting a new world record of 26.81% in 2022 [6,7]. However, as silicon solar cells approach their efficiency limits, the relative impact of degradation significantly increases. Peters et al. demonstrated a significant tradeoff between initial efficiency and degradation. Even a slight increase in the annual degradation rate can substantially increase the levelized cost of energy (LCOE) over the system's lifespan [8]. They suggest that newly installed PV modules should ideally have a lifetime of more than 50 years for the lowest LCOE [8]. Therefore, ensuring module stability and enhancing the failure tolerance of PV devices becomes crucial to meet these longevity requirements.

However, SHJ PV modules can still experience considerable performance degradation during long-term operation. Arruti et al. showed that SHJ modules in the field exhibit an average yearly degradation of 0.7%, primarily associated with failures caused by encapsulant discoloration, loss of passivation, moisture, potential-induced degradation (PID), and

* Corresponding author.
** Corresponding author.
E-mail addresses: chandany.sen@unsw.edu.au (C. Sen), b.hoex@unsw.edu.au (B. Hoex).

https://doi.org/10.1016/j.solmat.2023.112604
Received 13 August 2023; Received in revised form 26 September 2023; Accepted 16 October 2023

ultraviolet (UV) exposure [9]. Moisture, particularly under elevated temperatures, can accelerate module failures [10,11]. Segbefia et al. recently reported moisture-induced degradation in field-aged silicon modules, highlighting degradation in silicon solar cells, silver grids (Ag), ribbons, and solder bonds [12]. Our previous research identified four failure modes in SHJ glass-back sheet modules, all leading to significant efficiency degradation after damp heat testing in conditions of 85 °C and 85% room humidity (DH85) [13]. Encapsulants like ethylene vinyl acetate (EVA) and polyolefin (POE) are used for solar modules to protect the cells from external factors (moisture and contaminants). However, EVA, a mainstream and cost-effective material, has been found to be unstable for long-term applications as it generates acetic acid, which degrades module performance [14–17]. Acetic acid has been reported to contribute to metal contact degradation on crystalline silicon solar cells [18]. On the other hand, while POE offers superior protection, it comes at a relatively high cost and is not stable under ultraviolet (UV) illumination [19–22].

Sodium (Na) originating from soda-lime glass has been widely recognized as a critical factor in performance degradation [19,23,24]. Under high-voltage operation conditions, Na ions can permeate into solar cells, leading to PID commonly observed in PERC solar cells [23,25,26]. Even in the absence of high-voltage potential, Na ions can degrade a solar cell by deteriorating surface passivation or result in deterioration of the metal contact under a DH85 test [27–30]. We previously found that Na ions play a role in causing contact failures in SHJ solar cells [30]. Consequently, it is crucial to develop approaches preventing Na-induced degradation to ensure the long-term reliability of solar modules. Therefore, to prevent Na ions penetration into the cell and causing failure, some researchers have employed additional barrier layers on solar cells to shield them from environmental contaminants. Adachi et al. and Li et al. utilized a ~100 nm silicon oxide (SiO_2) layer as a barrier against Na ions, while Zahid et al. reported the use of AlO_x to protect PERC cells from PID [27,28,31]. Due to its low refractive index and stable structure, AlO_x also has great potential to be a suitable candidate as a Na ions barrier layer in protecting SHJ solar cells. To implement this application, thermal ALD appears to be a preferable approach as it allows dense and conformal double-side deposition without the need for plasma or high-temperature processes [32,33].

Moreover, Cl can originate from other sources, such as some types of soldering flux, which are typically used to join the ribbon wires to busbars, as demonstrated in the work by Nasta et al. [34]. In addition, human fingerprints can also contain Na and Cl elements, which can inadvertently contaminate solar cells if not handled properly [35,36]. Furthermore, NaCl can be found in various sources in the field, including rainwater, soil, dust, and seawater, which can penetrate and come into direct contact with solar cells and water [37–40]. Studies conducted by Segbefia et al. and Kumar et al. have shown that Na and Cl ions were present in the failed areas of solar modules that were installed outdoors for 20 years [41,42]. In addition, Oh et al. discovered that Cl was detected in the failed area of non-encapsulated cells that underwent DH testing [11]. These findings suggest that Na and Cl ions may have contributed to solar degradation. Na and Cl ions could have penetrated the modules through various means, including during the processing or encapsulation stages (such as through solar glass, soldering flux, or human fingerprints) or from exposure to the outdoor environment (such as rainwater, soil, or dust).

In this work, we show that the sensitivity of SHJ technology to NaCl can be tested at the solar cell level, resulting in significantly faster turnaround times compared to the DH85 test at the module level. Subsequently, we show that the contact failure and recombination loss caused by Na ions can be mitigated using an ultra-thin AlO_x barrier layer. This barrier layer is shown not to affect the subsequent module fabrication process. As high-volume ALD tools are routinely used for AlO_x deposition in photovoltaics, this novel method can swiftly be transferred to high-volume manufacturing.

2. Experimental details

All the samples used in the experiments were M10 half-cut n-type industrial silicon SHJ cells (182 mm × 91 mm) with 10 busbars. All the SHJ cells were processed from half-cut silicon wafers. The SHJ cells featured intrinsic hydrogenated amorphous silicon (i-a-Si:H) passivation layers on both sides and phosphorus-doped (n-a-Si:H) and boron-doped (p-a-Si:H) hydrogenated amorphous silicon layers on the front and rear sides, respectively. Both sides had an indium-doped tin oxide (ITO) layer with a screen-printed H-pattern silver grid. The samples were categorized into three groups: 1) Control group with no barrier layer and no exposure to NaCl (2 samples), 2) Group with no barrier layer and exposure to NaCl (8 samples), and 3) Group with barrier layer exposed to NaCl (8 samples).

For cells in Group 3, an ultra-thin AlO_x barrier layer (~10 nm) was deposited onto the full SHJ cells as shown in Fig. 1(a). The AlO_x layers were deposited in an industrial batch ALD reactor from Leadmicro (QL200). Trimethylaluminum (TMA) was used as the metal precursor and deionized water (DIW) as the oxidant. The pulse and purge periods for TMA and H_2O were set at 4 s and 12 s, respectively. The pulse and purge times for H_2O were 6 s and 14 s, respectively. To prevent overheating of the SHJ cells, the process temperature was maintained at 150 °C. Prior to the process, the samples underwent a 20-min pre-heat treatment to ensure temperature uniformity during the deposition process. To eliminate potential surface contamination, the samples were rinsed with deionized water and subsequently dried using a nitrogen gun. The samples were vertically positioned in the wafer boat to enable simultaneous deposition on both sides. Based on the growth rate per cycle, the estimated final thickness of the AlO_x layer was ~10 nm.

Next, all samples from Group 2 and Group 3 were subjected to a 0.9% weight sodium chloride (NaCl) solution, which was the source of Na used in the experiment. The experiment flow is shown in Fig. 1(b). For each sample, about 0.2 g NaCl solution was uniformly sprayed on the test surface, and the samples were dried naturally in a fume cupboard. Afterwards, control (Group 1) and contaminated samples (Groups 2 and 3) were placed separately in two wafer cassettes and loaded into an ASLi Environment chamber (T = 85 °C and a relative humidity of 85%). The climate chamber was cooled down to room temperature periodically to facilitate the characterization of the samples. During loading, transferring, and characterizing the samples, the samples are strictly controlled to minimize the potential NaCl contamination at the vertical edges of the SHJ cells.

Current-voltage (*I–V*) characteristics were measured using a LOANA solar cell analysis system from PV tools. A customized mask was utilized to accommodate the M10 half-cut cells, and the contact frame was adjusted to accommodate the 10 busbars. Reference cells were used to calibrate the light source, ensuring stable measurements of short-circuit current density (J_{sc}) following the DH85 test. Photoluminescence (PL) and series resistance (R_s) images were taken by a BTimaging R3 tool with a high open-circuit voltage lens. The luminescence images were additionally processed by LumiTools [43]. The transfer length method (TLM) was used to measure the sheet resistance (R_{sheet}) and contact resistivity (ρ_c) of c-Si(n)/i-a-Si:H/(n/p)-a-Si:H/ITO/metallization structures with customized samples using a PV-tools TLM-SCAN$^+$. Prior to the application of NaCl solution, 6 mm wide stripes were cut from the non-busbar regions of the SHJ cells using a FOBA M1000 scribing laser. Scanning electron microscopy (SEM) images were taken by FEI Nova NanoSEM 450 FE-SEM at 10 kV, with a working distance of approximately 5 mm. The detector used for energy dispersive spectroscopy (EDS) was the Oxford Instruments Ultim® Max, and the results were analyzed with AZtec software. This allowed for the identification of each element signal. To further characterize the metal contact, plasma focused ion beam (PFIB) was used to prepare some specific cross-sectional samples using the ThermoFisher Helios G4 PFIB UXe DualBeam system. X-ray photoelectron spectroscopy (XPS) was conducted by Thermo ESCALAB250Xi X-ray photoelectron spectrometer.

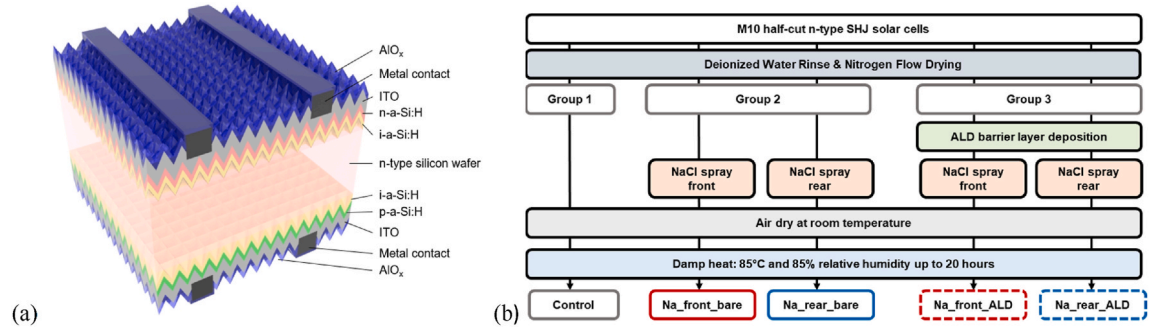

Fig. 1. (a) Schematic of SHJ solar cells with an AlO_x barrier layer (not to scale) and (b) experiment flow chart. For clarity, the AlO_x layer on the sides of the solar cell is not shown.

The X-ray source was mono-chromated Al K alpha (energy 1486.68 eV) with 120 W power, and the binding energy reference was C1s peak at 284.8 eV for adventitious hydrocarbon.

3. Results and discussion

3.1. Cell performance after AlO_x barrier layer deposition

Table 1 presents the *I–V* parameters before and after the deposition of the ALD AlO_x barrier layer on both sides of the cells. The *I–V* measurements were done twice at each state, and the average results are listed. No noteworthy changes were found in any of the parameters after the ALD AlO_x barrier layer was applied. The measured *PCE* of the cells remained at approximately 24%. No significant changes were observed in the luminescence images before and after the ALD process for all cells. Representative cells are shown in Fig. 2 for this study. This indicates that the introduction of an ultra-thin AlO_x barrier layer has no significant impact on the performance of the SHJ solar cells used in this work.

Fig. 3 presents top-view SEM and EDS analysis images of a specific region of the cells after the deposition of the AlO_x barrier layer. The EDS analysis results demonstrate the uniform distribution of aluminium (Al) on both the silver (Ag) finger and the transparent conducting oxide regions. However, there is a distinct difference in the oxygen (O) signal observed within and outside the finger region, likely due to the presence and impact of the oxygen-rich ITO layer.

3.2. Cell performance after DH85 test

3.2.1. I–V results

After 20 h of DH85, the control group experienced only minor *PCE* attenuation, and all the parameters, such as J_{sc}, V_{oc}, fill factor (*FF*), and R_s remained relatively stable, as shown in Fig. 4. These results indicate that high humidity at an elevated temperature for 20 h by itself does not degrade the SHJ cells. However, Na_front_bare and Na_rear_bare samples (i.e., solar cells without AlO_x barrier layer) showed a pronounced *PCE* degradation (~11.4%$_{rel}$ and ~33.5%$_{rel}$, respectively) after 20-h DH85. In the first 2 h, the R_s of the Na_front_bare samples increased by up to 143%$_{rel}$. This results in a decrease in *FF* from 82.5% to 76.9% and a notable decline in *PCE*. No substantial changes in J_{sc} and V_{oc} were observed for the Na_front_bare samples even after 20 h of the DH85 test.

Table 1
A comparison of average cell performance before and after the ALD process.

	Number of cells	*PCE* (%)	J_{sc} (mA/cm^2)	V_{oc} (mV)	*FF* (%)
Before ALD	10	24.0 ± 0.08	39.3 ± 0.08	741.9 ± 0.77	82.3 ± 0.33
After ALD	10	24.0 ± 0.09	39.2 ± 0.08	741.9 ± 0.67	82.6 ± 0.29

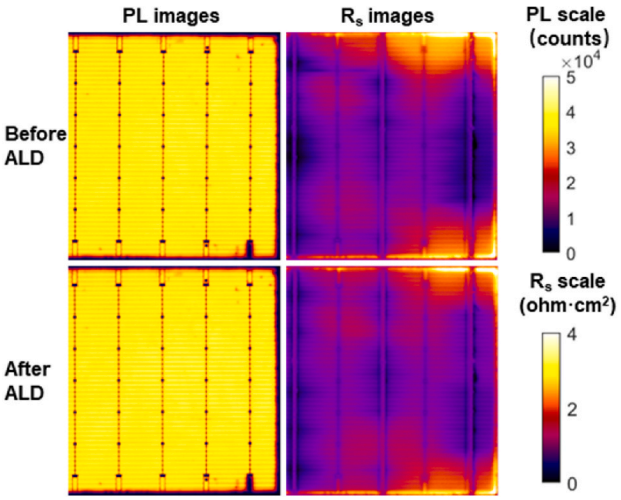

Fig. 2. PL and R_s images of SHJ solar cells before and after the ALD process.

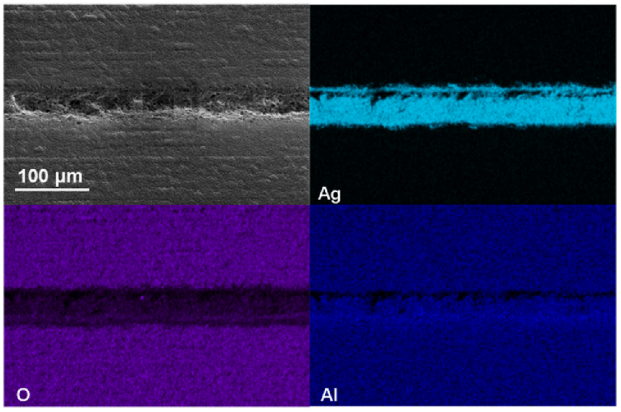

Fig. 3. Top-view SEM images and corresponding EDS mappings of Ag, O and Al of a SHJ solar cell with an AlO_x barrier layer.

After 20 h of DH85, the R_s of the Na_rear_bare sample increased linearly with time (~245.8%$_{rel}$ after 20 h of DH85 test) and was much higher than Na_front_bare (~199.3%$_{rel}$ after 20 h of DH85 test). The V_{oc} of Na_rear_bare started to decrease after 6 h with a loss of ~8.2%$_{rel}$ after 20 h of the DH85 test. On the other hand, only a minor drop in *PCE* (~3.3%$_{rel}$) was observed in the samples in Na_front_ALD and Na_rear_ALD (cells with AlO_x barrier layer) after 20 h of DH85 test. This drop in *PCE* can also be attributed to an increase in R_s, but the extent of loss (~3.1%$_{rel}$ for Na_front_ALD and ~2.8%$_{rel}$ for Na_rear_ALD after 20 h of

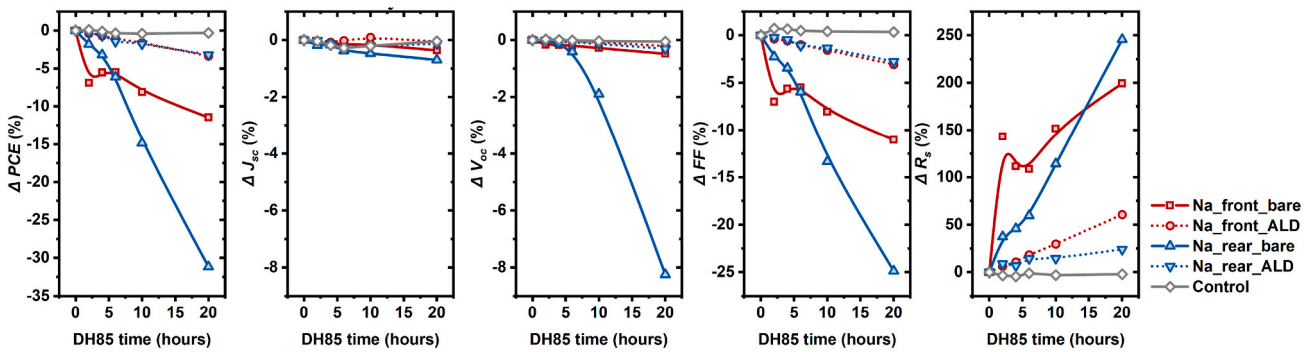

Fig. 4. Relative changes in *PCE*, J_{sc}, V_{oc}, *FF* and R_s as a function of DH85 duration for the groups shown in Fig. 1.

DH85 test) was significantly less than the cells without AlO_x barrier layer (Na_front_bare and Na_rear_bare). No significant loss of V_{oc} was observed in the samples in Na_rear_ALD. These results strongly suggest that ultra-thin AlO_x barrier layers can effectively shield the cells from NaCl-induced R_s and recombination issues, even after undergoing the DH85 test. Additionally, this protective measure ensures the continued high performance of the SHJ cells, highlighting the significance and effectiveness of the AlO_x barrier layer.

3.2.2. Photoluminescence results

Fig. 5 presents PL and R_s images of all SHJ cells before and after 20 h of DH85. No significant changes were recorded in PL and R_s images for the control group before and after 20 h of DH85 testing. These were consistent with the *I–V* results shown in Fig. 5 and indicated that the SHJ solar cells were stable after 20 h at DH85. The PL and R_s images showed clear differences for the Group 2 samples. A rapid increase in R_s ($\sim$121.3%$_{rel}$) was observed within the first 2 h for the Na_front_bare sample, quite uniformly distributed over the whole sample. For longer DH85 durations, the R_s kept increasing up to 196.0%$_{rel}$ after 20-h DH85. Combining with *I–V* results and PL images, the R_s variation indicates that NaCl likely affected the Ag fingers and/or the ITO layer but did not significantly affect the a-Si:H layers. The change in behaviour of R_s for Na_rear_bare cells differed from that of Na_front_bare cells. In the initial 2 h, only a slight non-uniformity increase in R_s was observed, located between the busbars. However, as the DH85 time increased to 6 h, the R_s at the edge area of the cells began to increase. This was complemented by a reduction in PL intensity in the same region, which will be discussed in the next section. After 20 h of DH85, the R_s image shows a further progression of the increase in R_s for the whole cell, especially at the edges where the R_s calculation method likely exceeded its valid range [44].

No substantial variations in PL count in the Na_front_bare cells were detected after 20 h of DH85. However, for Na_rear_bare cells, a significant decline in PL intensity ($\sim$88.3$_{rel}$) was observed after 20 h of the DH85 test. This decline originated at the cell's edge after 6 h of DH85 ($\sim$6.5%$_{rel}$) and gradually spread throughout the entire cell area. The rapid loss at the cell's edge can likely be attributed to the edge-exclusion during the ITO deposition on the rear side, as shown in Fig. 6. This leaves the doped a-Si:H layer directly exposed to NaCl and humidity, and the resulting reaction results in a significant loss in surface passivation.

In contrast, the Group 3 samples with an AlO_x barrier layer (Na_front_ALD and Na_rear_ALD) exhibited minimal to no significant changes in PL intensity even after 20 h of DH85, including at the edges. The results indicate that the AlO_x barrier layer effectively prevents recombination loss caused by the penetration of Na into the front or rear side of the cells. The variations in R_s images were $\sim$15.6%$_{rel}$ and $\sim$8.9%$_{rel}$ for Na_front_ALD and Na_rear_ALD, respectively, after the first 6 h of DH85 test. The slight changes seen in the samples with the ALD AlO_x barrier layer are so minimal that they can be considered insignificant when compared to those without the AlO_x barrier layer. However, after an extended test period, a slight non-uniform increase in R_s was observed in the edge regions, possibly attributed to the damage of AlO_x due to our repeated handling of the samples for characterization. Nevertheless, the overall outcome demonstrates that the AlO_x barrier layer also suppresses the increase in R_s caused by NaCl exposure.

These observations align with the earlier discussed *I–V* results, which

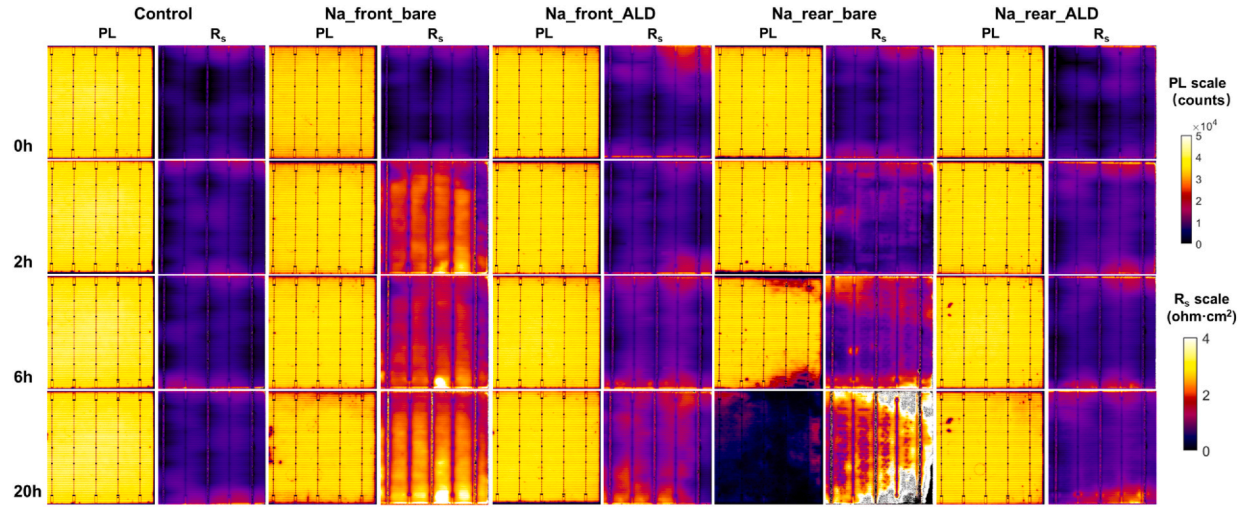

Fig. 5. PL and R_s images of SHJ solar cells from four experimental groups during the NaCl-induced DH85 test (0, 2, 6 and 20 h). See Fig. 1 for a description of the samples.

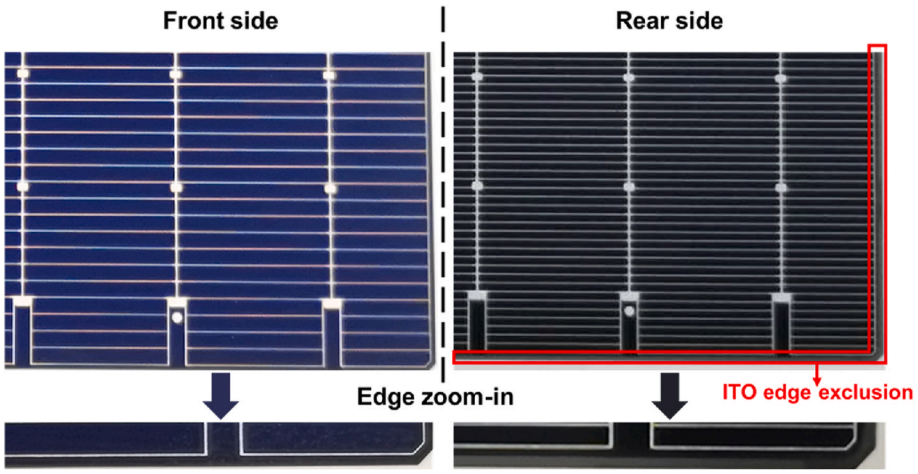

Fig. 6. Images of edge metallization and ITO design on the front and rear sides of industrial SHJ solar cells.

indicated a significant decrease in V_{oc}, particularly in Na_rear_bare cells and to a lesser extent in Na_front_bare cells, while Na_front_ALD and Na_rear_ALD cells remained unaffected. The changes in R_s images were also consistent with the *I–V* measurement results. These findings further confirm the efficacy of the AlO_x barrier layer as a protective measure against recombination and contact loss in SHJ cells.

3.2.3. TLM results

To gain a deeper understanding of the factors contributing to the increase in R_s after the DH85 test, specifically the ρ_c and R_{sheet}, TLM measurements were conducted on all cells before NaCl exposure and after 10 h of the DH85 test. Figs. 7 and 8 depict the average ρ_c and R_{sheet} of cells with (Na_front_ALD, Na_rear_ALD) and without (Na_front_bare, Na_rear_bare) AlO_x barrier layer that were exposed to NaCl before the DH85 test. The average ρ_c of cells without an AlO_x barrier layer increased from ~3.9 to ~4.4 mΩ cm^2 (Na_front_bare) and 1.0–2.4 mΩ cm^2 (Na_rear_bare) after 10 h of DH85 test (Fig. 7). However, no substantial changes in the average ρ_c were observed in cells with the AlO_x barrier layers. The ρ_c of Na_front_ALD and Na_rear_ALD cells were ~4.1 mΩ cm^2 and ~1.0 mΩ cm^2, respectively, before and after 10 h of DH85 test. There were no significant differences in the R_{sheet} of all cells (with or without the AlO_x barrier layer) before and after the DH85 test (Fig. 8), indicating that NaCl exposure may not have a significant impact on the ITO layer. The difference in sheet resistance between the Na_front_bare and Na_front-ALD samples can be attributed to a difference in the bulk doping of the n-type silicon wafer used for the SHJ solar cell. This suggests that the ITO layer might not be significantly impacted by NaCl exposure. The increase in R_s observed in cells without AlO_x barrier layer could thus be attributed primarily to the significant rise in ρ_c. In contrast, the AlO_x barrier layer provided robust protection for all cells, preventing increases in R_s.

3.2.4. SEM and EDS analysis

Fig. 9 presents both top-view and cross-section SEM images of the front contact of cells in the Na_front_bare and Na_front_ALD groups, as well as the rear contact of cells in the Na_rear_bare and Na_rear_ALD groups after 20 h of DH85. Also included in Fig. 9 are the front and rear contacts of a control cell. The images show that the front contact of Na_front_bare and the rear contact of Na_rear_bare, which were exposed to the NaCl solution, exhibit significant differences compared to the control group. The fingers that were exposed to the NaCl solution (e.g., Na_front_bare and Na_rear_bare) appeared less dense after 20 h of the DH85 test, and the contacts shown in Fig. 9 (b), (e), (h), and (k) appeared more porous and were more prone to delamination compared to the control samples. Additionally, the cross-section shape of the fingers was no longer the original trapezoid shape achieved through industrial screen printing, as seen in Fig. 9 (d) and (j). This relatively high porosity and potential delamination in the contacts may result in reduced conductance within the fingers and between the fingers and the ITO, consistent with the observed increase in contact resistance shown in Fig. 7.

As a result, these issues contribute to the increase in R_s of the SHJ solar cells. In contrast, the samples with an AlO_x barrier layer maintained dense structures within the fingers, as depicted in Fig. 9 (c), (f), (i), and (l). Only slight porosity was observed on the finger surface, and no evident porosity or delamination was observed inside the finger. The

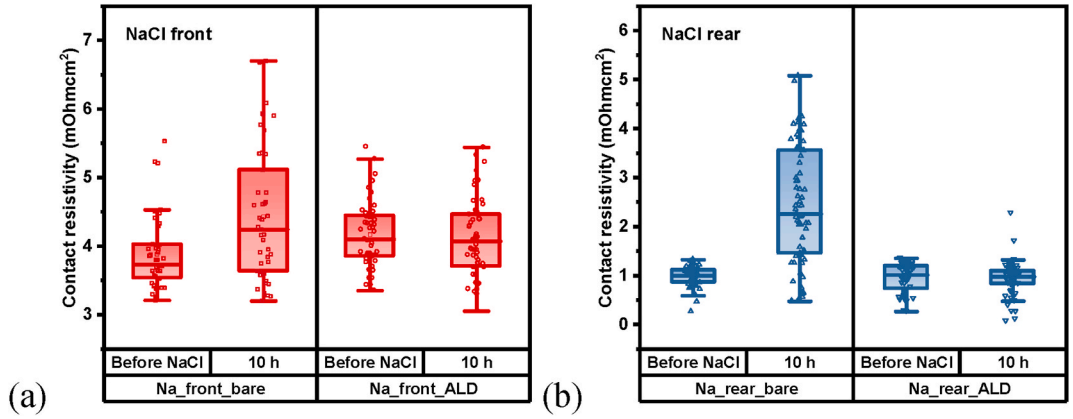

Fig. 7. The contact resistance (ρ_c) at the (a) front side and (b) rear side of the SHJ solar cell before and after 10 h of DH85. See Fig. 1 for a description of the samples.

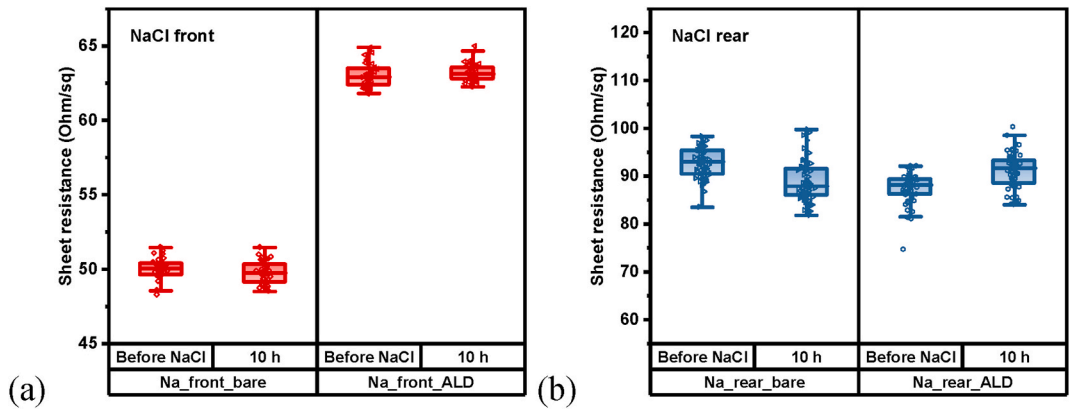

Fig. 8. The sheet resistance (R_{sheet}) variations before and after DH85 test of the bare and ALD samples with NaCl solution spray at the (a) front side and (b) rear side.

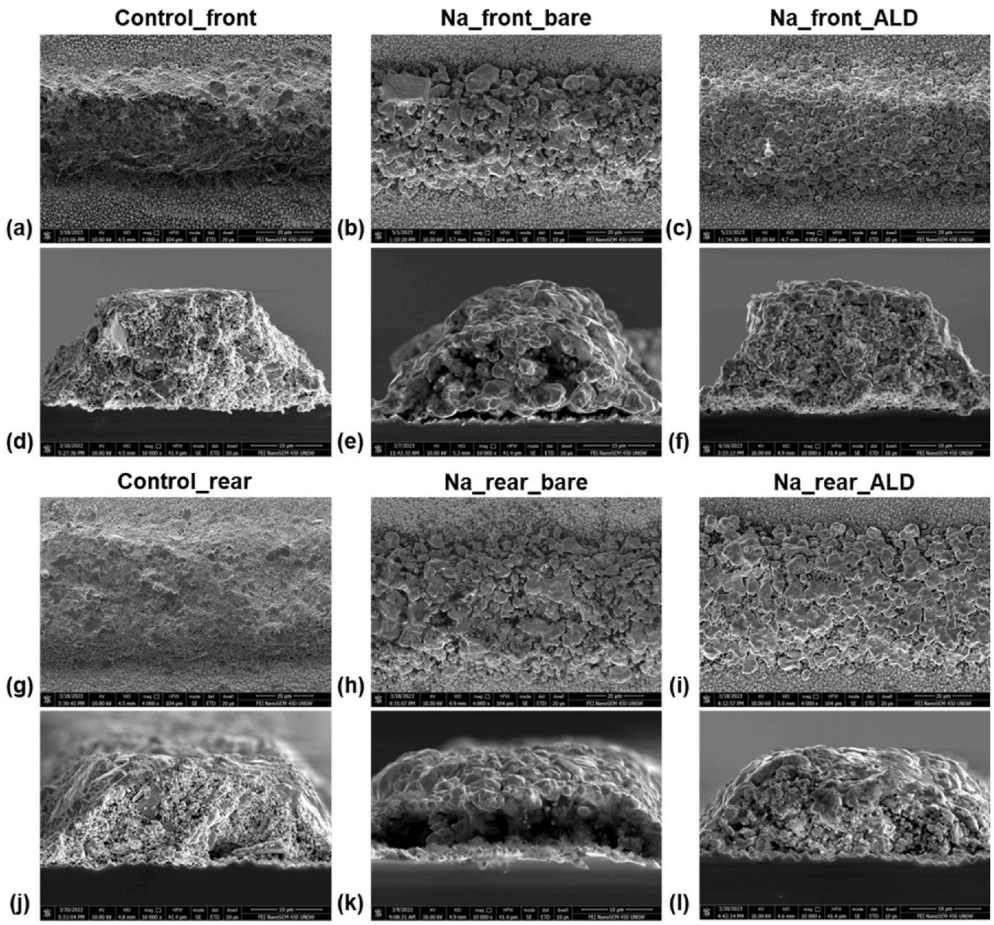

Fig. 9. Top-view SEM images of the finger regions of the (a) control, (b) Na_front_bare, (c) Na_front_ALD and (g) control, (h) Na_rear_bare, and (i) Na_rear_ALD samples. Cross-section SEM images of the finger regions of the (d) control, (e) Na_front_bare, (f) Na_front_ALD and (j) control, (k) Na_rear_bare, and (l) Na_rear_ALD sample. See Fig. 1 for a description of the samples.

trapezoidal shape of the fingers remained intact. This phenomenon was attributed to NaCl-related silver corrosion [45–48]. As a result, the adhesion between inner conductive particles in the fingers and the finger conductivity might have decreased, which is consistent with the rapid increase in R_s observed in the *I–V* measurements shown in Fig. 4.

3.3. Detailed investigation of the AlO_x barrier layer

3.3.1. P-FIB cross-section SEM images

To comprehensively understand the factors contributing to the failure and non-failure of certain contacts following DH85 with NaCl exposure, P-FIB was utilized to generate cross-section images, followed by SEM and EDS analyses, and the results are shown in Fig. 10. Three conditions were compared: 1) Control: cell without an AlO_x barrier layer and no pre-exposure to NaCl solution. These cells remained stable after the DH85 test, as depicted in Figs. 4 and 5. 2) Na_front_bare: cell without an AlO_x barrier layer but were pre-exposed to NaCl on the front side. This cell failed after the DH85 test, as shown in Figs. 4–6. 3) Na_front_ALD: cell with an AlO_x barrier layer and pre-exposure to NaCl on the front side. This cell did not fail after the DH85 test, as illustrated in

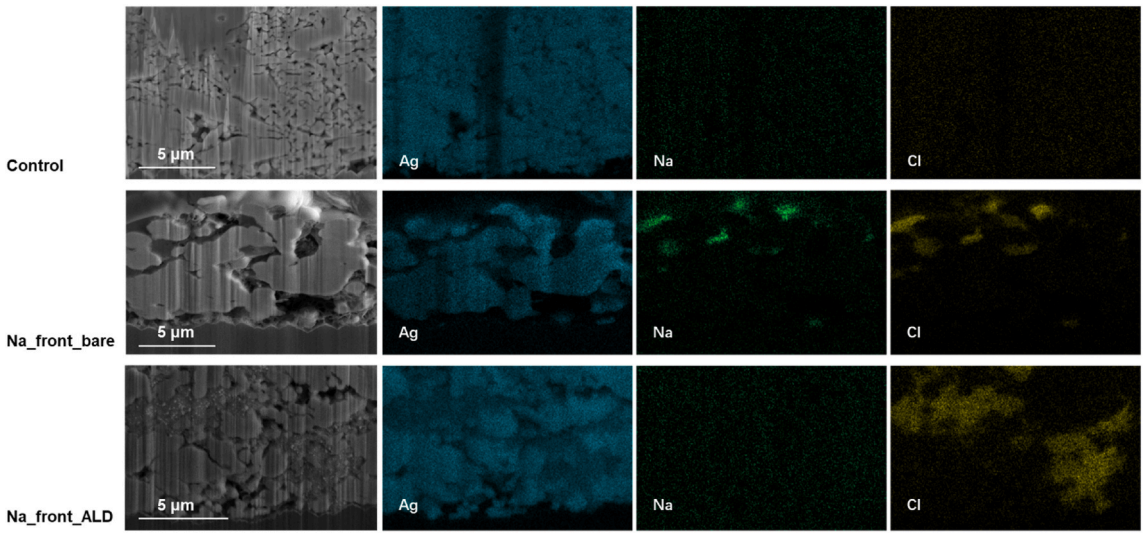

Fig. 10. Cross-section SEM images of control, Na_front_bare and Na_front_ALD samples prepared by P-FIB and corresponding EDS mappings of Ag, Na and Cl. See Fig. 1 for a description of the samples.

Figs. 4–6. All cells underwent 20 h of DH85.

The metal contact in both the control cell and the cell with the AlO_x barrier layer (Na_front_ALD) displayed a highly compact, less porous appearance, consisting of a mixture of small and large Ag particles that adhered firmly to the Si substrate. No noticeable Na and Cl signals were detected in the metal contact of the control cell. However, in the metal contact of the cell with the AlO_x barrier layer (Na_front_ALD), a significant amount of Cl was detected, while no trace of Na was observed. Conversely, the Na_front_bare sample displayed higher porosity, with mainly larger Ag particles observed in the metal contact. Additionally, the metal contact was found to be detached from the Si substrate. Furthermore, the EDS mapping revealed pronounced Na and Cl concentrations in certain regions within the finger bulk. These strong signals were predominantly observed at the interstices between the silver particles, with consistent positions of Na and Cl in the mapping. These results indicate that NaCl might have undergone an electrochemical reaction with the Ag and binder resin, resulting in the degradation and/or removal of the binder resin and corrosion of Ag [49–53]. The degradation/removal of the binder resin within the contact likely weakened cohesion within the low-temperature Ag paste, leading to the removal of binding material and/or smaller Ag particles from the contact [52,53]. Consequently, after 20 h of the DH85 test, only the larger Ag particles remained visible. The removal of binder resin and/or smaller Ag particles from the metal contact likely caused an increase in porosity. Moreover, the degradation and/or removal of the binder resin within the contact could have reduced the adhesive strength at the interface between the contact electrode and the Si substrate [40]. This weakening of the interface led to observed delamination. The rise in porosity within the contact electrode, along with the delamination of the finger electrode from the Si substrate interface, most likely resulted in reduced carrier collection efficiency, leading to an increase in R_s and a significant decline in performance.

It is important to acknowledge that EDS analyses are inherently characterized by localized observations, which pose a substantial challenge in achieving comprehensive element detection within a specific region. In our study, diligent efforts were devoted to obtaining clear images depicting the infiltration of NaCl into the contact, resulting in the dissolution of the binder resin and interfacial delamination. However, our efforts yielded less significant NaCl detection at the interface itself. In Fig. 10, a careful examination will reveal that we could detect NaCl, although its presence is not as pronounced as in other areas. This suggests the possibility of NaCl's ingress into the specific area, conceivably contributing to localized degradation and binder resin removal. Furthermore, it is plausible to infer that limited NaCl detection at the interface may be attributed to antecedent chemical reactions between NaCl and the binder resin, resulting in their mutual elimination before the commencement of our analytical examination. As a result, during the EDS examination, we may not have been able to detect these components due to their prior removal. Notwithstanding these challenges, it is noteworthy that we did ascertain elevated concentrations of NaCl at the interface in select alternate regions. Regrettably, constraints on manuscript length preclude the presentation of these additional findings herein.

The results of this research additionally indicate that the isolated infiltration of Cl into the contact is improbable to trigger swift and substantial deterioration of the metal contact. Nevertheless, when both Na and Cl penetrate the contact electrode, their combined presence can result in substantial deterioration of the contact, thereby contributing to an increase in R_s. The AlO_x barrier effectively prevented the penetration of Na ions into the cells.

3.3.2. *XPS analysis*

To gain further insights into the protective mechanisms of the AlO_x barrier layer, an XPS analysis was conducted. The width of XPS detection regions was wider than the finger width, so Figs. 11 and 12 show signals from the Ag metal and ITO regions of the solar cell. Fig. 11 (a) and (b) show the XPS results of the O1s peaks for samples without and with the AlO_x barrier layer, respectively. Four oxygen-related peaks were detected in the cells without the AlO_x barrier layer, consistent with the ITO analysis results reported by Donley et al. [54]. The O1s peak of the sample with the AlO_x barrier layer is primarily located at ~531.7 eV, indicating the presence of oxygen vacancies in the structure originating from Al–*O*–H bonds formed during the H_2O-assisted ALD process [55,56]. This also indicates that the ALD AlO_x layer is very uniform, as no XPS signal could be detected from the underlying ITO layer in this case. The Al2p peak shown in Fig. 12 (a) is centered around 74.6 eV and further confirms the existence of Al–*O*–H bonds [57].

Fig. 12 (a) and (b) depict the Al2p peak of cells featuring an AlO_x barrier layer, which were subjected to 20 h of DH85 test, with and without prior exposure to NaCl solution, respectively. The Al peak of the cells not exposed to NaCl before test was located at approximately 74.6 eV, whereas the peak of the cells that underwent NaCl treatment before DH85 test was observed at around 73.9 eV. This shift indicates a reduction in the concentration of OH^- ions or the coordination number of Al^{3+} ions within the film [58,59]. Note that samples in this study did not undergo long high-temperature annealing (above 250 °C); instead,

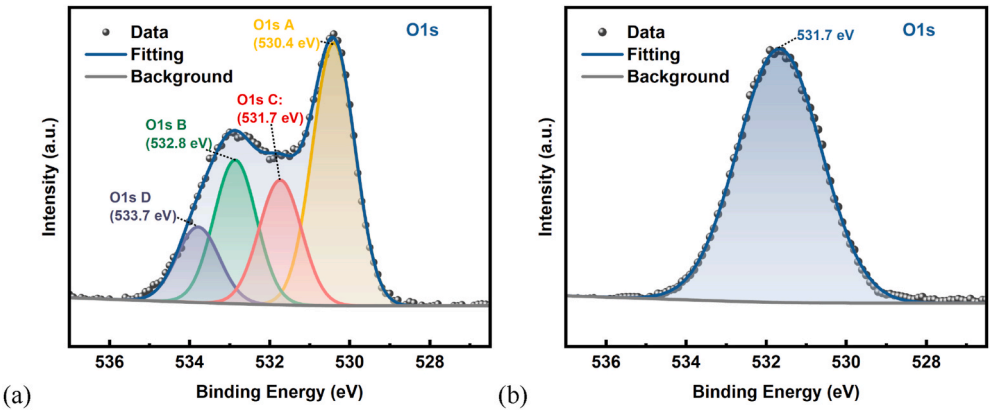

Fig. 11. XPS O1s spectra for SHJ solar cell surfaces before (a) and after (b) ALD AlO_x process.

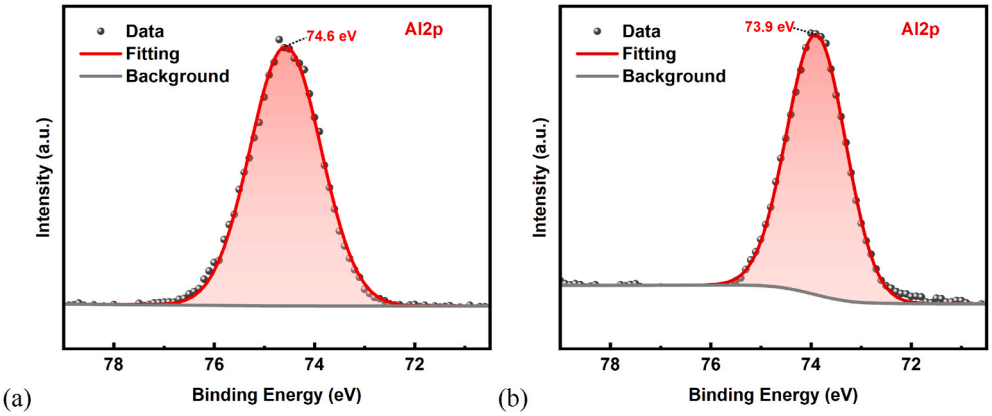

Fig. 12. XPS Al2p spectra for SHJ sample with ALD AlO_x barrier layer that underwent 20 h of DH85 without (a) and with (b) pre-exposure to NaCl.

the samples were treated under DH85 conditions. Consequently, the altered states of Al observed in the peak shift could be attributed to the infiltration of Na ions, which potentially induced changes in the Al states. As a result, the center peak position shifted. This mechanism further highlights the effectiveness of the AlO_x barrier layer in preventing the penetration of Na ions into the cells.

The XPS analysis also allowed us to extract the atomic ratio of Na to Cl present on the surface of the cells. Table 2 displays the atomic ratio of Na to Cl obtained from cells that were exposed to NaCl before the DH85 test, with and without the ALD AlO_x barrier layer. One would expect the Na to Cl atomic ratio to be around 1.0 as that is the ratio in the NaCl solution. However, the cells without the ALD AlO_x barrier layer had surface atomic ratios of Na to Cl of 2.3 and 1.4. On the other hand, the samples with AlO_x layers had significantly higher ratios of 7.4 and 8.7, proving the influential role of the ALD AlO_x barrier layer in blocking Na ions from entering the electrode fingers.

4. Conclusion

In summary, this study shows that SHJ solar cells are very sensitive to corrosion due to NaCl, resulting in a significant decrease in performance after a damp-heat test. By exposing SHJ cells to NaCl prior to DH85 testing, the corrosive and recombination-related degradation after DH85 testing can be significantly accelerated. We show considerable drops in the power conversion efficiency of up to ~33.5%$_{rel}$ after just 20 h of damp-heat testing. This rapid testing sheds light on the underlying mechanisms contributing to an increase in R_s and reduction in V_{oc}. Extensive characterizations provided compelling evidence suggesting that the degradation of R_s and V_{oc} likely occurs within the metal contact area and ITO layers. This may be instigated by the electrochemical reaction between Na, Cl ions and moisture during DH85 testing. It is important to note that it is not yet definitively established whether the presence of Na ions alone or in conjunction with Cl ions is the primary driving force behind the electrochemical reactions that result in extensive corrosion of the metal contacts and degradation loss. We are currently investigating the distinct roles played by Na cations and Cl anions in contributing to failures, and we will present the findings in future work. The simultaneous presence of Na and Cl ions on the contact surface, along with the potential penetration of these impurities within the metal contact, leads to corrosion of the silver contacts and possibly degrades and/or removes the binder resin within the contact. This degradation/removal of the binder resin seems to weaken the adhesive at the interface of metal contact and ITO/Si substrate, leading to the detachment of the metal contact. This degradation/removal of binder resin also likely increases the porosity of the contact. The increased porosity within the contact electrode and the delamination of the finger electrode from the Si substrate interface are likely responsible for reduced carrier collection efficiency and increased R_s, reducing the performance of SHJ cells after DH85 testing. The drop in V_{oc} can be attributed to NaCl reacting with the amorphous silicon layers of the SHJ cells at the edges of the rear side of the solar cell due to the edge-exclusion of the ITO deposition, causing an increase in recombination.

Table 2
Atomic ratio of Na to Cl of samples exposed to NaCl with and without AlO_x barrier layer after a 20-h DH85 test.

	Samples w/AlO_x	Samples w/o AlO_x
Measurement point 1	7.4	2.3
Measurement point 2	8.7	1.4

Based on this research, we propose that a reduced edge exclusion at the rear side can potentially enhance the reliability of such industrial SHJ solar cells. Fortunately, we show that the introduction of a 10-nm ALD AlO_x barrier layer proves to be highly effective in preventing all detected failures during our accelerated DH85 testing. This barrier layer effectively preserves SHJ cell performance by preventing the Na ions from reaching the metal contact and the amorphous silicon and ITO. This barrier layer thereby safeguards the overall performance of SHJ solar cells. We believe that a thin AlO_x barrier layer (~10 nm) is a compatible and feasible approach to enhance SHJ solar cell stability and holds promising potential for direct integration into industrial production lines.

CRediT authorship contribution statement

Xinyuan Wu: Writing – original draft, Visualization, Methodology, Investigation, Formal analysis, Data curation, Conceptualization. **Chandany Sen:** Writing – review & editing, Supervision, Methodology, Investigation, Formal analysis, Data curation. **Haoran Wang:** Investigation, Formal analysis. **Xutao Wang:** Investigation, Formal analysis. **Yutong Wu:** Resources, Investigation, Formal analysis. **Muhammad Umair Khan:** Writing – review & editing, Investigation. **Lizhong Mao:** Resources, Investigation. **Fangdan Jiang:** Resources, Investigation, Funding acquisition. **Tao Xu:** Resources, Investigation. **Guangchun Zhang:** Resources, Investigation. **Bram Hoex:** Writing – review & editing, Visualization, Supervision, Project administration, Funding acquisition, Formal analysis, Conceptualization.

Declaration of competing interest

The authors declare the following financial interests/personal relationships which may be considered as potential competing interests: Bram Hoex reports financial support was provided by Australian Renewable Energy Agency (ARENA 1–060 Extension project). Bram Hoex, Chandany Sen, Xinyuan Wu have patent #Australian application number 2023900037 issued to University of New South Wales.

Data availability

Data will be made available on request.

Acknowledgements

This work received support from the Australian Government through the Australian Renewable Energy Agency (ARENA 1–060 Extension project). However, the Australian Government does not accept responsibility for the views, information, or advice expressed in this research. The authors would like to acknowledge the Electron Microscope Unit at The University of New South Wales (UNSW), specifically Dr Yin Yao and Dr Charlie Kong, for their scientific and technical assistance and access to the facilities of the Australian Microscopy & Microanalysis Research Facility. The authors acknowledge the surface analysis laboratory, Solid State & Elemental Analysis Unit (SSEAU), Mark Wainwright Analytical Centre (MWAC), and UNSW for the support of XPS analysis. The authors also express their gratitude for the support provided by the Solar Industrial Research Facility (SIRF) at UNSW. Furthermore, Xinyuan Wu acknowledges the support received from the Australian Government Research Training Program (RTP) Scholarship.

References

[1] D. Yan, et al., Polysilicon passivated junctions: the next technology for silicon solar cells? Joule 5 (4) (2021) 811–828, https://doi.org/10.1016/j.joule.2021.02.013, 2021/04/21/.
[2] X. Zhang, et al., Mass production of crystalline silicon solar cells with polysilicon-based passivating contacts: an industrial perspective, Prog. Photovoltaics Res. Appl. 31 (4) (2023) 369–379, https://doi.org/10.1002/pip.3618, 2023-04-01.
[3] Y. Liu, et al., High-efficiency silicon heterojunction solar cells: materials, devices and applications, Mater. Sci. Eng. R Rep. 142 (2020), 100579, https://doi.org/10.1016/j.mser.2020.100579, 2020-10-01.
[4] M. Hermle, F. Feldmann, M. Bivour, J.C. Goldschmidt, S.W. Glunz, Passivating contacts and tandem concepts: approaches for the highest silicon-based solar cell efficiencies, Appl. Phys. Rev. 7 (2) (2020), 021305, https://doi.org/10.1063/1.5139202, 2020-06-01.
[5] T.G. Allen, J. Bullock, X. Yang, A. Javey, S. De Wolf, Passivating contacts for crystalline silicon solar cells, Nat. Energy 4 (11) (2019-11-01 2019) 914–928, https://doi.org/10.1038/s41560-019-0463-6.
[6] M.A. Green, et al., Solar cell efficiency tables (Version 61), Prog. Photovoltaics Res. Appl. 31 (1) (2023) 3–16, https://doi.org/10.1002/pip.3646, 2023-01-01.
[7] H. Lin, et al., Silicon heterojunction solar cells with up to 26.81% efficiency achieved by electrically optimized nanocrystalline-silicon hole contact layers, Nat. Energy (2023-05-04 2023), https://doi.org/10.1038/s41560-023-01255-2.
[8] I.M. Peters, J. Hauch, C. Brabec, P. Sinha, The value of stability in photovoltaics, Joule 5 (12) (2021) 3137–3153, https://doi.org/10.1016/j.joule.2021.10.019, 2021/12/15/.
[9] O. Arriaga Arruti, A. Virtuani, C. Ballif, Long-term performance and reliability of silicon heterojunction solar modules, Prog. Photovoltaics Res. Appl. (2023), https://doi.org/10.1002/pip.3688, 2023-03-02.
[10] T.H. Kim, N.C. Park, D.H. Kim, The effect of moisture on the degradation mechanism of multi-crystalline silicon photovoltaic module, Microelectron. Reliab. 53 (9) (2013/09/01/2013) 1823–1827, https://doi.org/10.1016/j.microrel.2013.07.047.
[11] W. Oh, et al., The degradation of multi-crystalline silicon solar cells after damp heat tests, Microelectron. Reliab. 54 (9) (2014/09/01/2014) 2176–2179, https://doi.org/10.1016/j.microrel.2014.07.071.
[12] O.K. Segbefia, N. Akhtar, T.O. Sætre, Moisture induced degradation in field-aged multicrystalline silicon photovoltaic modules, Sol. Energy Mater. Sol. Cell. 258 (2023/08/15/2023), 112407, https://doi.org/10.1016/j.solmat.2023.112407.
[13] C. Sen, et al., Four failure modes in silicon heterojunction glass-backsheet modules, Sol. Energy Mater. Sol. Cell. 257 (2023/08/01/2023), 112358, https://doi.org/10.1016/j.solmat.2023.112358.
[14] M.C.C. de Oliveira, A.S.A.D. Cardoso, M.M. Viana, V.d.F.C. Lins, The causes and effects of degradation of encapsulant ethylene vinyl acetate copolymer (EVA) in crystalline silicon photovoltaic modules: a review, Renew. Sustain. Energy Rev. 81 (2018) 2299–2317.
[15] F. Pern, A. Czanderna, EVA degradation mechanisms simulating those in PV modules, in: AIP Conference Proceedings, vol. 268, American Institute of Physics, 1992, pp. 445–452, 1.
[16] P. Klemchuk, M. Ezrin, G. Lavigne, W. Holley, J. Galica, S. Agro, Investigation of the degradation and stabilization of EVA-based encapsulant in field-aged solar energy modules, Polym. Degrad. Stabil. 55 (3) (1997) 347–365.
[17] M. Le Bras, S. Bourbigot, B. Revel, Comprehensive study of the degradation of an intumescent EVA-based material during combustion, J. Mater. Sci. 34 (1999) 5777–5782.
[18] N. Iqbal, et al., Impact of acetic acid exposure on metal contact degradation of different crystalline silicon solar cell technologies, Sol. Energy Mater. Sol. Cell. 250 (2023/01/15/2023), 112089, https://doi.org/10.1016/j.solmat.2022.112089.
[19] K. Hara, S. Jonai, A. Masuda, Crystalline Si photovoltaic modules functionalized by a thin polyethylene film against potential and damp-heat-induced degradation, RSC Adv. 5 (20) (2015-01-01 2015) 15017–15023, https://doi.org/10.1039/c4ra13360a.
[20] D.B. Sulas-Kern, et al., Electrochemical degradation modes in bifacial silicon photovoltaic modules, Prog. Photovoltaics Res. Appl. (2021), https://doi.org/10.1002/pip.3530, 2021-12-28.
[21] A. Ammala, A. Hill, P. Meakin, S.J. Pas, T.W. Turney, Degradation studies of polyolefins incorporating transparent nanoparticulate zinc oxide UV stabilizers, J. Nanoparticle Res. 4 (1–2) (2002) 167–174.
[22] D. Mellor, A. Moir, G. Scott, The effect of processing conditions on the uv stability of polyolefins, Eur. Polym. J. 9 (3) (1973) 219–225.
[23] W. Luo, et al., Potential-induced degradation in photovoltaic modules: a critical review, Energy Environ. Sci. 10 (1) (2017-01-01 2017) 43–68, https://doi.org/10.1039/c6ee02271e.
[24] S.P. Harvey, J.A. Aguiar, P. Hacke, H. Guthrey, S. Johnston, M. Al-Jassim, Sodium accumulation at potential-induced degradation shunted areas in polycrystalline silicon modules, IEEE J. Photovoltaics 6 (6) (2016-11-01 2016) 1440–1445, https://doi.org/10.1109/jphotov.2016.2601950.
[25] S. Yamaguchi, C. Yamamoto, K. Ohdaira, A. Masuda, Comprehensive study of potential-induced degradation in silicon heterojunction photovoltaic cell modules, Prog. Photovoltaics Res. Appl. 26 (9) (2018-09-01 2018) 697–708, https://doi.org/10.1002/pip.3006.
[26] M.U. Khan, et al., Supercharging cell-level potential-induced degradation (PID) testing using a salt-enriched hybrid polymer layer, Sol. Energy Mater. Sol. Cell. 260 (2023/09/15/2023), 112479, https://doi.org/10.1016/j.solmat.2023.112479.
[27] X. Li, et al., Potential-free sodium-induced degradation of silicon heterojunction solar cells, Prog. Photovoltaics Res. Appl. (2023), https://doi.org/10.1002/pip.3698.
[28] D. Adachi, T. Terashita, T. Uto, J.L. Hernández, K. Yamamoto, Effects of SiOx barrier layer prepared by plasma-enhanced chemical vapor deposition on improvement of long-term reliability and production cost for Cu-plated amorphous Si/crystalline Si heterojunction solar cells, Sol. Energy Mater. Sol. Cell. 163 (2017/04/01/2017) 204–209, https://doi.org/10.1016/j.solmat.2016.12.029.

[29] X. Li, et al., Highly crystallized tungsten doped indium oxide film stabilizes silicon heterojunction solar cells in sodium environment, Sol. Energy Mater. Sol. Cell. 233 (2021/12/01/2021), 111387, https://doi.org/10.1016/j.solmat.2021.111387.
[30] C. Sen, et al., The role of Na+ contamination in humidity-induced degradation in silicon HJT cells, in: Presented at the Asia Pacific Solar Research Conference 2022, Newcastle, Australia, 2022 [Online]. Available: https://apvi.org.au/solar-research-conference/wp-content/uploads/2023/02/Sen-The-role-of-Na-contamination-in-humidity-induced-degradation-in-silicon-HJT-cells.pdf.
[31] M.A. Zahid, H. Yousuf, Y. Kim, E.C. Cho, J. Yi, A novel approach to utilize Al2O3 and polyolefin encapsulant as an optical and electrical materials to mitigate potential-induced of PV modules, Opt. Mater. 133 (2022/11/01/2022), 113022, https://doi.org/10.1016/j.optmat.2022.113022.
[32] W.-C. Wang, et al., Surface passivation of efficient nanotextured black silicon solar cells using thermal atomic layer deposition, ACS Appl. Mater. Interfaces 5 (19) (2013) 9752–9759.
[33] P. Saint-Cast, et al., High-efficiency c-Si solar cells passivated with ALD and PECVD aluminum oxide, IEEE Electron. Device Lett. 31 (7) (2010-07-01 2010) 695–697, https://doi.org/10.1109/led.2010.2049190.
[34] M.A. Nasta, G. Hill, D. Campbell, Contaminant particles in electronic solder fluxes, Solder. Surf. Mt. Technol. 2 (1) (1990) 5–7.
[35] G.M. Wilson, et al., The 2020 photovoltaic technologies roadmap, J. Phys. Appl. Phys. 53 (49) (2020), 493001.
[36] C.G. Worley, S.S. Wiltshire, T.C. Miller, G.J. Havrilla, V. Majidi, Detection of visible and latent fingerprints using micro-X-ray fluorescence elemental imaging, J. Forensic Sci. 51 (1) (2006-01-01 2006) 57–63, https://doi.org/10.1111/j.1556-4029.2005.00006.x.
[37] Z. Sharp, D. Draper, The chlorine abundance of Earth: implications for a habitable planet, Earth Planet Sci. Lett. 369 (2013) 71–77.
[38] T.E. Graedel, W. Keene, The budget and cycle of Earth's natural chlorine, Pure Appl. Chem. 68 (9) (1996) 1689–1697.
[39] A.J. Magenheim, A.J. Spivack, P.J. Michael, J.M. Gieskes, Chlorine stable isotope composition of the oceanic crust: implications for Earth's distribution of chlorine, Earth Planet Sci. Lett. 131 (3–4) (1995) 427–432.
[40] C. Sen, et al., Accelerated damp-heat testing at the cell-level of bifacial silicon HJT, PERC and TOPCon solar cells using sodium chloride, Sol. Energy Mater. Sol. Cell. 262 (2023/10/15/2023), 112554, https://doi.org/10.1016/j.solmat.2023.112554.
[41] O.K. Segbefia, A.G. Imenes, T.O. Sætre, Moisture ingress in photovoltaic modules: a review, Sol. Energy 224 (2021/08/01/2021) 889–906, https://doi.org/10.1016/j.solener.2021.06.055.
[42] S. Kumar, R. Meena, R. Gupta, Imaging and micro-structural characterization of moisture induced degradation in crystalline silicon photovoltaic modules, Sol. Energy 194 (2019/12/01/2019) 903–912, https://doi.org/10.1016/j.solener.2019.11.037.
[43] D.N.R. Payne, C. Vargas, Z. Hameiri, S.R. Wenham, D.M. Bagnall, An advanced software suite for the processing and analysis of silicon luminescence images, Comput. Phys. Commun. 215 (2017/06/01/2017) 223–234, https://doi.org/10.1016/j.cpc.2017.02.012.
[44] H. Kampwerth, T. Trupke, J. Weber, Y. Augarten, Advanced luminescence based effective series resistance imaging of silicon solar cells, Appl. Phys. Lett. 93 (20) (2008), 202102.
[45] Y. Yoon, J.D. Angel, D.C. Hansen, Atmospheric corrosion of silver in outdoor environments and modified accelerated corrosion chambers, Corrosion 72 (11) (2016) 1424–1432.
[46] C. Levard, et al., Effect of chloride on the dissolution rate of silver nanoparticles and toxicity to *E. coli*, Environ. Sci. Technol. 47 (11) (2013-06-04 2013) 5738–5745, https://doi.org/10.1021/es400396f.
[47] H. Ha, J. Payer, The effect of silver chloride formation on the kinetics of silver dissolution in chloride solution, Electrochim. Acta 56 (7) (2011) 2781–2791.
[48] J. Park, S.H. Park, S.-H. Jeong, J.-Y. Lee, J.Y. Song, Corrosion behavior of silver-coated conductive yarn, Front. Chem. 11 (2023).
[49] H. Wang, X. Quan, Q. Zeng, Y. Wu, B. Liao, X. Guo, Electrochemical corrosion and protection of low-temperature sintered silver nanoparticle paste in NH4Cl solution, J. Mater. Sci. Mater. Electron. 32 (10) (2021-05-01 2021) 13748–13760, https://doi.org/10.1007/s10854-021-05952-0.
[50] T.E. Graedel, Corrosion mechanisms for silver exposed to the atmosphere, J. Electrochem. Soc. 139 (7) (1992) 1963, https://doi.org/10.1149/1.2221162, 1992/07/01.
[51] H. Lin, G.S. Frankel, W.H. Abbott, Analysis of Ag corrosion products, J. Electrochem. Soc. 160 (8) (2013-01-01 2013) C345–C355, https://doi.org/10.1149/2.055308jes.
[52] Z. Feng, et al., Salt crystallization-assisted degradation of epoxy resin surface in simulated marine environments, Prog. Org. Coating 149 (2020/12/01/2020), 105932, https://doi.org/10.1016/j.porgcoat.2020.105932.
[53] L.-H. Tam, L. He, C. Wu, Molecular dynamics study on the effect of salt environment on interfacial structure, stress, and adhesion of carbon fiber/epoxy interface, Compos. Interfac. 26 (5) (2019-05-04 2019) 431–447, https://doi.org/10.1080/09276440.2018.1506901.
[54] C. Donley, et al., Characterization of Indium−Tin oxide interfaces using X-ray photoelectron spectroscopy and redox processes of a chemisorbed probe molecule: effect of surface pretreatment conditions, Langmuir 18 (2) (2002-01-01 2002) 450–457, https://doi.org/10.1021/la011101t.
[55] O. Jankovský, P. Šimek, D. Sedmidubský, Š. Huber, M. Pumera, Z. Sofer, Towards highly electrically conductive and thermally insulating graphene nanocomposites: Al2O3–graphene, RSC Adv. 4 (15) (2013) 7418–7424, https://doi.org/10.1039/c3ra45069d, 2013-11-15.
[56] I. Iatsunskyi, M. Kempiński, M. Jancelewicz, K. Załęski, S. Jurga, V. Smyntyna, Structural and XPS characterization of ALD Al2O3 coated porous silicon, Vacuum 113 (2015/03/01/2015) 52–58, https://doi.org/10.1016/j.vacuum.2014.12.015.
[57] L. Zheng, et al., Improvement of Al2O3 films on graphene grown by atomic layer deposition with pre-H2O treatment, ACS Appl. Mater. Interfaces 6 (10) (2014) 7014–7019, https://doi.org/10.1021/am501690g, 2014-05-28.
[58] T. Tsuchida, H. Takahashi, X-ray photoelectron spectroscopic study of hydrated aluminas and aluminas, J. Mater. Res. 9 (11) (1994-11-01 1994) 2919–2924, https://doi.org/10.1557/jmr.1994.2919.
[59] P.K. Nayak, M.N. Hedhili, D. Cha, H.N. Alshareef, High performance In2O3 thin film transistors using chemically derived aluminum oxide dielectric, Appl. Phys. Lett. 103 (3) (2013), 033518.